

Article

High-Responsivity Photovoltaic Photodetectors Based on MoTe₂/MoSe₂ van der Waals Heterojunctions

Hao Luo, Bolun Wang, Enze Wang, Xuewen Wang, Yufei Sun and Kai Liu * 

State Key Laboratory of New Ceramics and Fine Processing, School of Materials Science and Engineering, Tsinghua University, Beijing 100084, China; shamanhao@outlook.com (H.L.); wangbolunwbl@163.com (B.W.); wez17@mails.tsinghua.edu.cn (E.W.); wangxw16@mails.tsinghua.edu.cn (X.W.); syf16@mails.tsinghua.edu.cn (Y.S.)

* Correspondence: liuk@tsinghua.edu.cn; Tel.: +86-10-62799182

Received: 4 June 2019; Accepted: 17 June 2019; Published: 19 June 2019



Abstract: Van der Waals heterojunctions based on transition metal dichalcogenides (TMDs) show promising potential in optoelectronic devices, due to the ultrafast separation of photoexcited carriers and efficient generation of the photocurrent. Herein, this study demonstrated a high-responsivity photovoltaic photodetector based on a MoTe₂/MoSe₂ type-II heterojunction. Due to the interlayer built-in potential, the MoTe₂/MoSe₂ heterojunction shows obvious photovoltaic behavior and its photoresponse can be tuned by the gate voltage due to the ultrathin thickness of the heterojunction. This self-powered photovoltaic photodetector exhibits an excellent responsivity of 1.5 A W⁻¹, larger than previously reported TMDs-based photovoltaic photodetectors. Due to the high-efficiency separation of electron-hole pairs and ultrafast charge transfer, the light-induced on/off ratio of current switching is larger than 10⁴ at zero bias, and the dark current is extremely low (~10⁻¹³ A). These MoTe₂/MoSe₂ type-II heterojunctions are expected to provide more opportunities for future nanoscale optoelectronic devices.

Keywords: MoTe₂; MoSe₂; van der Waals heterojunction; photovoltaic photodetector; responsivity; detectivity

1. Introduction

The recent advances in two-dimensional (2D) layered materials have provided brand-new platforms and thoughts for future novel, high-performance, and multi-functional electronic and optoelectronic applications. Of all these 2D materials, transition metal dichalcogenides (TMDs) including MoS₂, WSe₂, MoSe₂, MoTe₂, etc. have attracted a great deal of attention because of their peculiar characteristics, such as thickness-dependent bandgaps, valley-selective optical coupling, and large exciton binding energy [1,2]. Due to the lack of dangling bonds on the surface, heterojunctions can be assembled by any kinds of 2D materials through van der Waals (vdW) stacking without considering the lattice mismatch [3]. Recently, many novel physical phenomena and features are observed in these 2D-based vdW heterojunctions, including negative differential conductance, ultrafast carrier transport, interlayer excitons, moiré excitons, ballistic transport, etc. [4–8].

Depending on band structures of semiconductors, three types of heterojunctions can be obtained: Straddling gap (type-I), staggered (type-II), and broken gap (type-III). Among these heterojunctions, type-II junctions are superior candidates for optoelectronic devices, due to the high-efficiency separation of photoexcited carriers. In particular, type-II heterojunctions based on layered TMDs show promising potential in solar cells and photodetectors, due to their strong photon absorption, efficient generation of photocurrents, and ultrafast transfer of charges [9]. Furthermore, owing to the ultrathin thickness and steep interfacial charge-carrier gradient, 2D vdW heterojunctions exhibit distinct tunability in

carrier density and band alignment, providing an alternative method for multi-functional electronic and optoelectronic devices. For instance, high external quantum efficiency (40–60%) is achieved in atomically thin GaTe/MoS₂ and WSe₂/MoS₂ p-n heterojunctions [10,11]. On the other hand, gate-tunable photovoltaic response is also observed in WSe₂/MoS₂ heterojunctions [11,12], and photovoltaic photodetectors based on MoTe₂/MoS₂ vdW heterojunctions are also demonstrated [13–15]. However, the responsivity of these photovoltaic devices is still low (<0.5 A W⁻¹), because of the small photocurrent flow without external bias driving. Therefore, more efforts are necessary to improve the performance of TMDs-based photovoltaic photodetectors for future nanoscale optoelectronic devices.

In this work, a high-responsivity photovoltaic photodetector based on a MoTe₂/MoSe₂ type-II vdW heterojunction is demonstrated. Due to the interlayer built-in potential, the MoTe₂/MoSe₂ heterojunction shows obvious photovoltaic behavior, and this photoresponse can be tuned by the gate voltage due to the ultrathin thickness of the heterojunction. This self-powered photodetector exhibits an excellent responsivity of 1.5 A W⁻¹, larger than previously reported TMDs-based photodetectors. Due to the high efficiency of separation of electron-hole pairs and the ultrafast charge transfer, the light-induced on/off ratio of the current switching is larger than 10⁴ at zero bias, and the dark current is extremely low (~10⁻¹³ A).

2. Materials and Methods

Device fabrication: The MoTe₂/MoSe₂ heterojunctions are fabricated by exfoliation and deterministic transfer methods. The few-layer MoTe₂ and MoSe₂ are exfoliated onto clean SiO₂/Si substrate from MoTe₂ and MoSe₂ crystal (2D semiconductors Inc.) using scotch tape. Afterwards, the polymethyl methacrylate (PMMA) liquid is spin coated on the substrate with few-layer MoTe₂ flakes with a rotating speed of 2000 r s⁻¹. After annealed with 150 °C for 2 mins, the substrate with PMMA is soaked into the 1 mol L⁻¹ KOH solution to remove the Si substrate. Then, the PMMA film with MoTe₂ flakes is floated and transferred onto polydimethylsiloxane (PDMS) with MoTe₂ flakes upside. After locating the appropriate thin MoTe₂ flakes on the PMMA/PDMS film, the film with MoTe₂/PMMA/PDMS structure is turned upside down and aligned with the target few-layer MoSe₂ using a transfer stage under an optical microscope. Once the desired alignment is achieved, the MoTe₂/PMMA/PDMS film structure is pressed against the substrate with MoSe₂ compactly. Lastly, the substrate with MoTe₂/MoSe₂/PMMA/PDMS film structure is soaked into acetone to dissolve the PMMA in company with removing the PDMS and the stacked MoTe₂/MoSe₂ heterojunction is achieved. The contact electrodes were patterned by an electron beam lithography. Then, 20 nm Pt and 50 nm Au are deposited on MoTe₂ and 20 nm Ti and 50 nm Au on MoSe₂ by electron beam evaporation. After the liftoff process, the devices are annealed at 200 °C for 2 h in Ar/H₂ (H₂: 10%) atmosphere to remove the residual organics and improve the electrode contact between the semiconductor and metals. Herein, the MoTe₂/MoSe₂ heterojunctions are fabricated by the wet transfer process. In addition, dry transfer is also an alternative method to fabricate clean 2D devices [16].

Device characterization: Micro Raman spectra is measured by iHR550 spectrometer (HORIBA, Tokyo, Japan) with a 532 nm excitation wavelength. The thickness of materials are measured by an atomic force microscope (AFM, BRUKER Multimode 8, Germany) in contact mode using a silicon tip (on nitride lever). The surface potential is measured in the mode of a Kelvin probe force microscope (KPFM) with two scans, i.e., the morphology scan and interleave scan. During the interleave scan, the tip is lifted up and kept at a constant height over the sample surface based on the morphology scan. An alternating bias is applied on the tip to measure the surface potential of the sample. Electrical measurements are carried out on B1500A semiconductor device analyzer (KEYSIGHT, Santa Rosa, CA, USA) under an ambient environment in the dark and illumination condition (LED light source). The time-resolved photoresponse is also measured on B1500A under an illumination of LED light with the shutter switched between on and off for a period of 5 s.

3. Results and Discussion

3.1. Device Structure and Material Characterizations of MoTe₂/MoSe₂ Heterojunctions

MoTe₂/MoSe₂ vdW heterojunctions are fabricated by mechanical exfoliation and deterministic transfer methods. Figure 1a shows the schematic of the MoTe₂/MoSe₂ heterojunction device. During electrical measurements, the source terminal (S) is grounded and the voltage is applied on the drain terminal (D) or n⁺-Si gate. An optical image of the MoTe₂/MoSe₂ device is displayed in Figure 1b. As MoTe₂ layer has a smaller bandgap, to obtain good light absorption, the exfoliated few-layer MoTe₂ flake is transferred on MoSe₂ to form a heterojunction through vdW stacking. Metal Pt is deposited on MoTe₂ layer to achieve good electrical contact and efficient holes injection. For MoSe₂ layer, metal Ti is used as a contact electrode to ensure ohmic contact. The details on the device fabrication are depicted in the experimental section. According to the AFM results, the MoTe₂ and MoSe₂ thickness are 3.2 nm (~4 layer) and 5.1 nm (~7 layer), respectively, as shown in Figure 1c. Figure 1d shows the Raman spectra of a few-layered MoTe₂ and MoSe₂ nanoflakes as well as the overlapped junction zone. Two peaks are observed at 241.6 cm⁻¹ and 249.8 cm⁻¹ in the Raman spectra of MoSe₂, which are attributed to out-of-plane vibrational mode A_{1g} and two-phonon vibrational mode E_{2g}² (a second-order Raman mode due to the longitudinal acoustic phonons at the M point in the Brillouin), respectively [17]. In the Raman spectra of MoTe₂, three peaks appear at 171.8 cm⁻¹, 234.9 cm⁻¹, and 290.8 cm⁻¹, corresponding to the out-of-plane vibrational mode A_{1g}, in-plane vibrational mode E_{2g}¹, and bulk in-active phonon vibrational mode B_{2g}¹ [18]. In the MoTe₂/MoSe₂ heterojunction zone, the typical vibration peaks of both MoTe₂ and MoSe₂ are also observed, implying the existence of two different materials. In particular, the peak intensity of MoTe₂ and MoSe₂ in the overlapped region are attenuated, possibly due to the ultrafast charge transfer process in the MoTe₂/MoSe₂ vdW heterojunction [13].

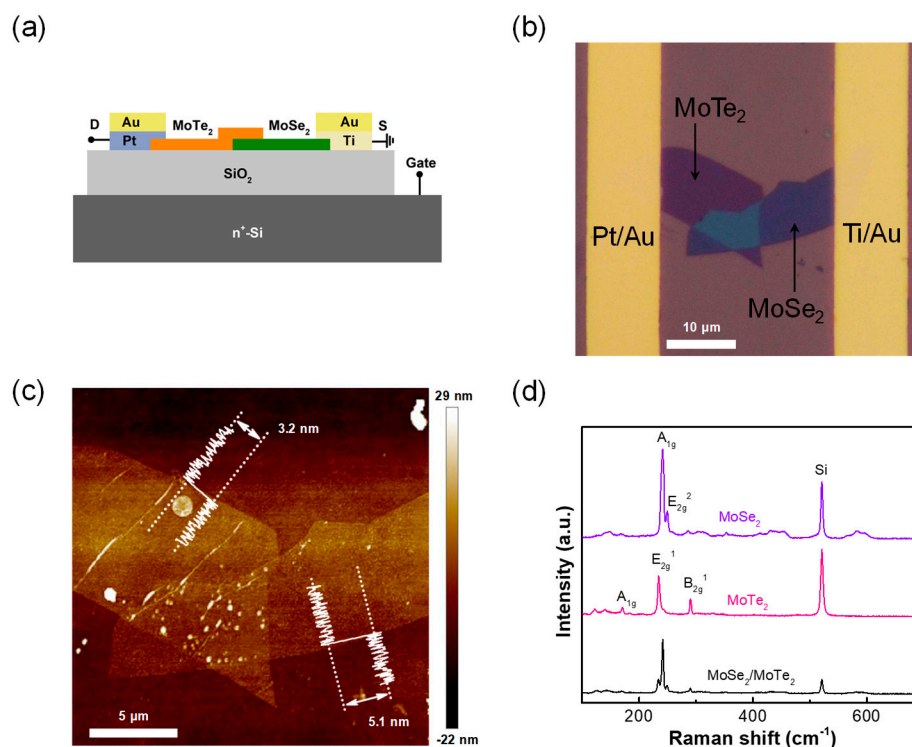


Figure 1. The schematic and characterizations of MoTe₂/MoSe₂ heterojunctions. (a) Schematic of the MoTe₂/MoSe₂ heterojunction device. During electrical measurements, the source terminal (S) is grounded while the bias is applied on the drain terminal (D) or Si gate. (b) An optical image of the MoTe₂/MoSe₂ heterojunction, in which the MoTe₂ is stacked on the MoSe₂. (c) AFM image of the MoTe₂/MoSe₂ heterojunction, the thickness of MoTe₂ and MoSe₂ are 3.2 and 5.1 nm, respectively. (d) Raman spectra of MoTe₂, MoSe₂, and MoTe₂/MoSe₂ heterojunction zone.

To verify the charge transfer and the existence of built-in potential at the interlayer of MoTe₂/MoSe₂ heterojunction under thermal equilibrium, KPFM measurements are conducted to qualitatively analyze the surface potential distribution. Figure 2a shows the KPFM map of the MoTe₂/MoSe₂ heterojunction, distinct potential difference is observed between MoTe₂ and the MoSe₂ region, and the potential of MoTe₂ layer is lower than that of MoSe₂ layer. The average surface potential difference between MoTe₂ and MoSe₂ layer is ~90 mV, as shown in Figure 2b, suggesting that the Fermi level of MoTe₂ is 90 meV lower than MoSe₂. This confirms the existence of a charge transfer and built-in potential at the heterojunction interlayer, which is the basis of a rectification heterojunction device. According to the reported band energy and the KPFM results, this study can obtain a schematic of band diagrams of MoTe₂/MoSe₂ before contact and after contact, as demonstrated in Figure 2c,d. Considering that it is difficult to quantitatively determine the width of the depletion region, the authors qualitatively analyzed the band bending of MoTe₂ and MoSe₂, and the thickness of materials, and the width of the depletion region are not considered exactly in Figure 2c,d. Unlike conventional heterojunctions, 2D heterojunctions are formed through vdW stacking, i.e., there are vdW gaps between two materials. Therefore, there is a vacuum band between MoTe₂ and MoSe₂ after contact. The conduction band minimum of a few-layered MoTe₂ and MoSe₂ are ~3.8 eV and ~4.1 eV, the bandgap of a few-layered MoTe₂ and MoSe₂ are 1.0–1.1 eV and 1.1–1.55 eV, respectively [19–21]. Therefore, a type-II vdW heterojunction is formed after the MoTe₂ is stacked on MoSe₂, which is beneficial for optoelectronic devices due to the high efficiency separation of photoexcited carriers. Herein, the MoTe₂ and MoSe₂ layer are intrinsically p-type and n-type doped. As the higher Fermi level of MoSe₂, electrons (holes) will transfer from MoSe₂ (MoTe₂) to MoTe₂ (MoSe₂) until the equilibrium state is achieved. As a result, electrons (holes) depletion is formed at the MoSe₂ (MoTe₂) side. Thus, the energy bands of MoSe₂ (MoTe₂) bend upward (downward), as shown in Figure 2d. Due to the charge transfer, the built-in electric field at the heterojunction interlayer has a direction from MoSe₂ to MoTe₂.

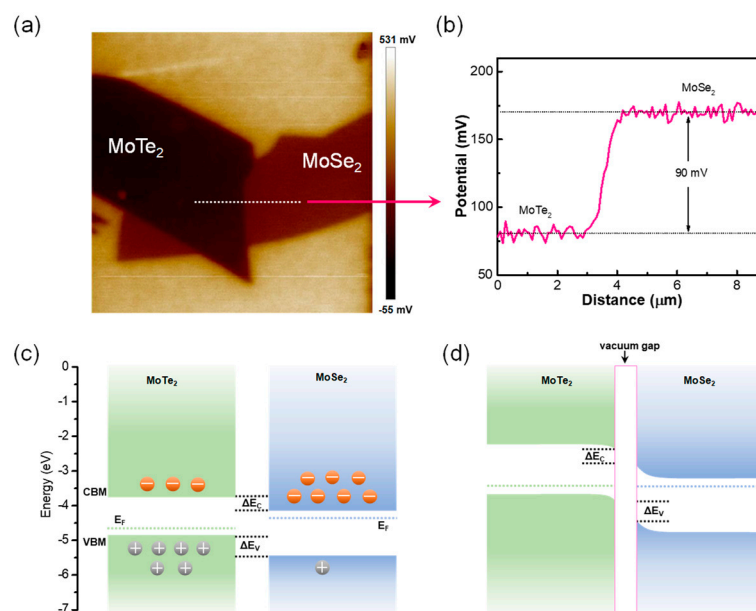


Figure 2. The surface potential distribution and energy band diagrams of MoTe₂/MoSe₂ heterojunction. (a) KPFM image of the MoTe₂/MoSe₂ heterojunction. (b) Dependence of potential on the distance along the white dotted line marked zone in Figure 2a, providing a potential difference of 90 mV. (c) The schematic of a band diagram of isolated MoTe₂ and MoSe₂ (i.e., before contact). CBM, VBM, ΔE_C , ΔE_V , and E_F denote the conduction band minimum, valence band maximum, conduction band offset, valence band offset, and Fermi level. (d) The schematic of a band diagram of the MoTe₂/MoSe₂ (i.e., after contact).

3.2. Electrical Behaviors of MoTe₂/MoSe₂ Heterojunctions

This study further investigated the electrical behavior of the MoTe₂/MoSe₂ heterojunctions. Figure 3a shows the linear scale of current-voltage (I_{DS} - V_{DS}) characteristics of MoTe₂/MoSe₂ heterojunction measured at different gate-source voltages (V_{GS}). Two insets show the logarithmic scale of I_{DS} - V_{DS} curves and the transfer curve at $V_{DS} = 1$ V. The transfer curve shows an anti-ambipolar feature with a large on/off current ratio of ~ 300 , which has also been observed in most 2D-based heterojunction devices [22,23]. The MoTe₂/MoSe₂ device exhibits distinct rectification behaviors at all V_{GS} , demonstrating the gate-tunable current rectifying characteristics. Under $V_{GS} = -20$ V, the heterojunction shows a large ratio of forward to reverse $I_{DS} \sim 540$ at $V_{DS} = \pm 1.5$ V, which is better than most reported TMD-based heterojunctions [12,14]. The rectification ratio gradually decreases when V_{GS} is larger or smaller than -20 V (Figure 3b), according with the anti-ambipolar feature of the transfer curve (inset of Figure 3a). Under a reverse bias, I_{DS} displays exponential increases and finally saturates as V_{DS} decreases. Under a forward bias, I_{DS} shows exponential increases at low bias regions and linearly increases at a large bias due to the series resistance.

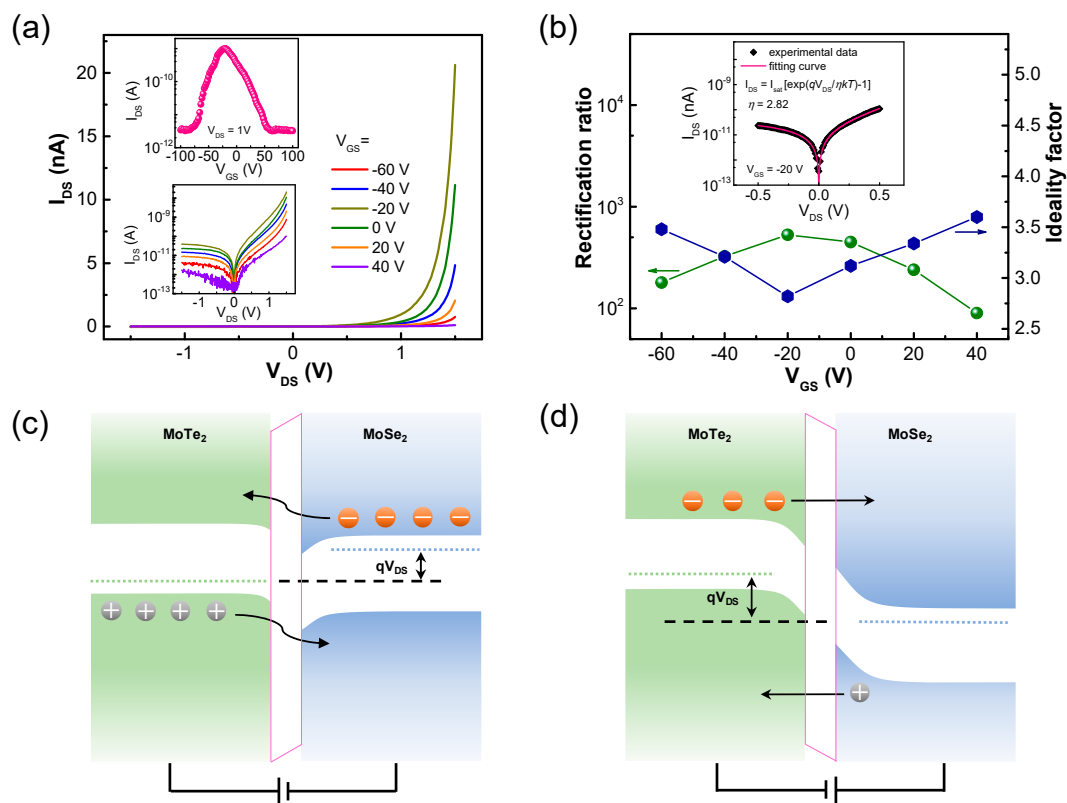


Figure 3. Electrical characteristics of MoTe₂/MoSe₂ heterojunction and related band diagrams. (a) I_{DS} - V_{DS} characteristics in linear scale measured at different gate voltage V_{GS} . Two insets show the logarithmic scale of I_{DS} - V_{DS} curves and the transfer curve at $V_{DS} = 1$ V. (b) The dependence of the rectification ratio and ideality factor on V_{GS} . The inset shows the fitting of the I_{DS} - V_{DS} characteristic with the Shockley equation for the extraction of the ideality factor. The band diagram of carrier transport mechanisms of the MoTe₂/MoSe₂ heterojunction under (c) forward bias and (d) reverse bias.

Figure 3c,d demonstrate the schematic band diagram of MoTe₂/MoSe₂ heterojunction at a forward and reverse bias. Under a forward bias, the equilibrium state of MoTe₂/MoSe₂ heterojunction is broken and the potential barrier at the interlayer becomes lower so that the carriers can easily be overcome. Electrons (holes) in the MoSe₂ (MoTe₂) are injected to the MoTe₂ (MoSe₂) side, leading to a large diffusion current in the heterojunction. The forward current will increase linearly when the applied bias is larger than the interlayer barrier height. On the contrary, under a negative bias, the interlayer

barrier will increase. This increased built-in field will enhance the transport of minority carriers, forming a small reverse drift current. For heterojunctions based on 2D materials, the reverse current is mainly influenced by the surface trap effect, high level injection, series resistance, and the current generated in the barrier region. Of all these factors, the current generated in the barrier region should be the leading contributor in our MoTe₂/MoSe₂ heterojunctions. In the equilibrium state, the rate of carrier generation equals to the recombination by defect recombination centers in the space charge region. Under a reverse bias, the electron-hole pairs will be separated by the enhanced built-in field before they are recombined, forming a net generation rate. As the reverse bias increases, the increased net generation rate leads to the enhancement of a reverse current. Due to the ultra-thin feature of MoTe₂/MoSe₂ heterojunction, the width of the space charge region is equal to the thickness of the junction zone in the case of full depletion [14,24]. Therefore, the further increase of the reverse bias cannot enhance the built-in electric field due to the lack of mobile charges. Therefore, considering that there is a potential drop along the lateral region of the heterojunction, the increase of the reverse bias will result in a large lateral electric field, which can sweep the carriers away effectively, forming a large reverse current in the heterojunctions.

To further understand the electrical behavior of the MoTe₂/MoSe₂ heterojunctions, the ideality factor is extracted from the I_{DS}-V_{DS} curves at a low bias region, through fitting the I_{DS} with the Shockley equation [25]:

$$I_{DS} = I_{sat} \left[\exp\left(\frac{qV_{DS}}{\eta kT}\right) - 1 \right] \quad (1)$$

where I_{sat} is the reverse saturation current, q is the unit charge, η is the ideality factor, k is the Boltzmann constant, T is the absolute temperature. As displayed in the inset of Figure 3b, the measured I_{DS}-V_{DS} curve can be perfectly fitted by the Shockley equation, providing an ideality factor of 2.82 at V_{GS} = -20 V. For ideal diodes, the ideality factor varies between 1.0 and 2.0, depending on the recombination of the minority carrier in the neutral region or space charge region of the junction. Nevertheless, the ideality factor is usually larger than 2.0 in experiments, which is suggested to be resulting from the interface diffusion, heterojunction interface with high strain, high series resistance or parasitic rectifying junction within the device [26–28]. For our MoTe₂/MoSe₂ heterojunction, the ideality factor may be mainly influenced by the lateral series resistance. As the ideality factor shows an increase trend when the V_{GS} is larger or smaller than -20 V (Figure 3b), corresponding with the transfer characteristic (inset of Figure 3a), in which the lateral resistance (I_{DS}) of the heterojunction increases (decreases) when V_{GS} is larger or smaller than -20 V.

3.3. Opto-Electrical Behaviors of MoTe₂/MoSe₂ Heterojunctions

This study further investigated the optoelectronic characteristics of the MoTe₂/MoSe₂ heterojunctions. Figure 4a shows the I_{DS}-V_{DS} curves under a white light illumination (LED source), where I_{DS} increases significantly with the increasing power density of the light. The device reveals a dramatic photovoltaic behavior, forming an open-circuit voltage (V_{OC}) and a short-circuit current (I_{SC}). The photovoltaic feature of the device results from the energy gradient in the type-II band alignment and the built-in electric field at the MoTe₂/MoSe₂ interlayer (Figure 1d), which can effectively separate the photoexcited electron-hole pairs. The photoexcited electrons and holes near the MoTe₂/MoSe₂ interlayer can be transferred to and accumulated at the MoSe₂ and the MoTe₂ side, respectively, leading to the formation of V_{OC}. Once the device is short circuited, the accumulated electrons and holes at the two sides will recombine rapidly through the external circuit, leading to the formation of I_{SC}. Figure 4b shows the I_{SC} (i.e., current at zero external bias) as a function of light power density. The I_{SC} strongly depends on the light intensity, and can be perfectly fitted by a power law equation $I_{SC} \sim \alpha P^\beta$, where α is a scaling constant, and β is an exponent [13]. Typically, a larger exponent value means a higher efficiency of the photoexcited electron-hole pairs under the light illumination. The fitting delivers an almost straight line with $\beta = 0.84$, which is slightly smaller than that of junctions with low interface trap states ($\beta \sim 1$) [29,30], indicating the presence of some trap states between the Fermi level and the

conduction band edge and these trap states play a role in carriers generation and the recombination process [31]. The inset of Figure 4b shows the dependence of V_{OC} on the power density. The V_{OC} increases from 17.5 mV to 58.3 mV as the power density changes from $20 \mu\text{W mm}^{-2}$ to $310 \mu\text{W mm}^{-2}$. Theoretically, the open-circuit voltage is determined by the Fermi level difference (i.e., built-in potential) between two semiconductor materials. Herein, the maximum V_{OC} is still smaller than the Fermi level difference (90 mV) between the MoTe_2 and the MoSe_2 layer as estimated by the KPFM measurements, suggesting that the performance of $\text{MoTe}_2/\text{MoSe}_2$ heterojunction may be further improved through optimizing the junction interface.

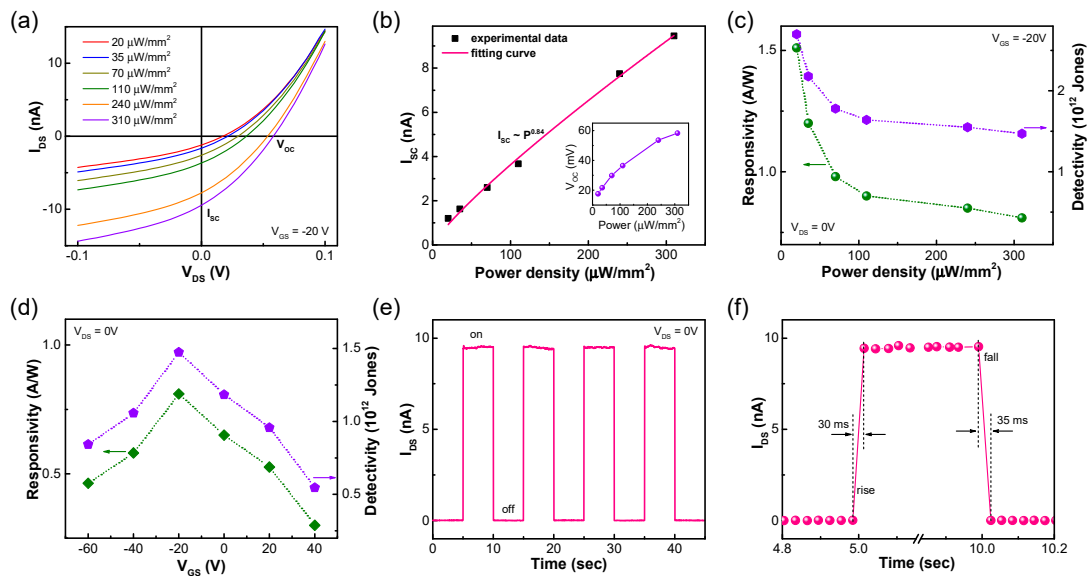


Figure 4. The photoresponse of $\text{MoTe}_2/\text{MoSe}_2$ heterojunction. (a) I_{DS} - V_{DS} characteristics of the $\text{MoTe}_2/\text{MoSe}_2$ heterojunction under white light illumination with different power density, showing dramatic photovoltaic effect. (b) I_{SC} as a function of light power density, which can be fitted by a power law equation. The inset shows dependence of V_{OC} on the power density. (c) The responsivity and detectivity of the $\text{MoTe}_2/\text{MoSe}_2$ heterojunction as a function of power density. (d) The responsivity and detectivity of the $\text{MoTe}_2/\text{MoSe}_2$ heterojunction as a function of V_{GS} . (e) The time response of the $\text{MoTe}_2/\text{MoSe}_2$ heterojunction with incident light switches on and off for a period of 5 s at $V_{DS} = 0$ V, demonstrating a self-driven behavior and high-efficient separation of photoexcited carriers. (f) The enlarged dynamic time response behavior of the $\text{MoTe}_2/\text{MoSe}_2$ heterojunction, suggesting a fast rise time (<30 ms) and fall time (<35 ms).

Owing to the photovoltaic effect, the $\text{MoTe}_2/\text{MoSe}_2$ heterojunctions can work as high-performance photovoltaic photodetectors. Therefore, this study evaluated the responsivity and the detectivity of the $\text{MoTe}_2/\text{MoSe}_2$ device at $V_{DS} = 0$ V, i.e., the device always works in the low injection regime, as shown in Figure 4c. The responsivity is defined as $R = I_{ph}/P_{in}$, in which P_{in} is the power of incident illumination, I_{ph} is the photocurrent. I_{ph} is calculated by equation: $I_{ph} = I_{illum} - I_{dark}$, where I_{illum} and I_{dark} is the current measured under light illumination and dark conditions. The responsivity is estimated to be 0.81 A W^{-1} with a power density of $310 \mu\text{W mm}^{-2}$ at $V_{GS} = -20$ V. Assuming the total noise is dominated by the shot noise from the dark current [32], the detectivity is defined by the equation, $D = R / (2qJ_{DS})^{1/2}$, where J_{DS} is the density of dark current. The detectivity is estimated to be 1.47×10^{12} Jones with a power density of $310 \mu\text{W mm}^{-2}$ at $V_{GS} = -20$ V. As shown in Figure 4c, both the responsivity and detectivity can be further enhanced though reducing the light intensity, and a maximum responsivity and detectivity of 1.5 A W^{-1} and 2.7×10^{12} Jones are obtained at a power density of $20 \mu\text{W mm}^{-2}$. This phenomenon might be due to the trap states on the material surface and at the heterojunction interlayer. Under a weak power density, the photoexcited electrons will be captured by the trap states, which reduces the recombination of carriers and augmenting the life-time

of photoexcited holes, resulting a higher responsivity and detectivity [33]. With increasing power density, however, the available trap states will be reduced, leading to the saturation of photoresponse. The authors have also fabricated two other MoTe₂/MoSe₂ heterojunctions, which show a maximum responsivity of 1.39 and 1.65 A W⁻¹, respectively, closing to the above MoTe₂/MoSe₂ device.

As our MoTe₂/MoSe₂ heterojunctions show gate-tunable rectification behavior, the photoresponse can be tuned by the gate voltage, as shown in Figure 4d. The responsivity and detectivity achieve the maximum at V_{GS} = -20 V and show a decreasing trend when V_{GS} is smaller or larger than -20 V, in accordance with the gate-tunable rectification behavior and the anti-ambipolar feature. A similar gate-tunable photoresponse has also been observed in MoS₂/WSe₂ heterojunction devices, which display a photovoltaic responsivity of 0.011–0.12 A W⁻¹ [11,12]. Figure 4e shows the temporal photoresponse of the MoTe₂/MoSe₂ device under the illumination of white light with a power density of 310 μW mm⁻² at V_{DS} = 0 V and V_{GS} = -20 V. The photocurrent (i.e., I_{SC}) can be generated and annihilated instantly with switching the light on and off, which shows an on/off ratio as high as 3.0 × 10⁴. The real response times at rise and fall should be less than 30 ms and less than 35 ms, respectively (Figure 4f), because the measured time interval between two adjacent data points are limited by the temporal resolution of the equipment. The fast response reveals a high-efficiency generation and separation of electron-hole pairs for the MoTe₂/MoSe₂ heterojunction.

The comparisons of figure of merits with other 2D photovoltaic photodetectors are shown in Table 1, where the responsivity, detectivity, and rise time are included. It is obvious that our MoTe₂/MoSe₂ photodetectors exhibit much higher responsivity in combination with high detectivity performance. The response speed of the MoTe₂/MoSe₂ photodetectors is comparable with part of the reported MoTe₂/MoS₂ heterojunctions and the MoTe₂/CdS mixed-dimensional photodetectors, but slower than the GaSe/GaSb photodetectors.

Table 1. Comparisons of figure of merits of MoTe₂/MoSe₂ photodetector with other photovoltaic photodetectors. Gr, graphene.

Materials	Responsivity (A W ⁻¹)	Detectivity (Jones)	t _{rise} (ms)
MoTe ₂ /MoS ₂ [13–15]	0.046–0.32	1.06 × 10 ⁸	0.06–68
WSe ₂ /MoS ₂ [11,12,34]	0.011–0.25		
GaSe/GaSb [35]	0.12	2.2 × 10 ¹²	0.032
MoTe ₂ /CdS [36]	<0.06		<50
Gr/WS ₂ /Gr [9]	0.1		
WSe ₂ p-n [37]	<0.016		
This work	1.5	2.7 × 10¹²	<30

4. Conclusions

Based on the intrinsic p-type MoTe₂ and n-type MoSe₂, this study fabricated MoTe₂/MoSe₂ p-n heterojunctions with type-II band alignment through van der Waals stacking. The electronic and optoelectronic performance of the devices have been investigated in detail. The MoTe₂/MoSe₂ heterojunction exhibits gate-tunable rectification behavior and a large rectification ratio of ~540, and an ideality factor of ~2.82 is achieved. Due to the type-II band alignment and the built-in potential at the interlayer, the MoTe₂/MoSe₂ heterojunction shows excellent photovoltaic effects with a photocurrent on/off ratio of >10⁴. As a self-powered photovoltaic photodetector, the MoTe₂/MoSe₂ heterojunction shows a high responsivity of 1.5 A W⁻¹ and a large detectivity of 2.7 × 10¹² Jones, featuring a high-performance, energy-efficient detector. These excellent performances suggest that the van der Waals heterojunctions have great potential in novel, high-performance electron and optoelectronic applications.

Author Contributions: H.L. and K.L. designed the experiments, analyzed the data, and wrote the manuscript. H.L. fabricated heterojunction devices, conducted the electrical and optoelectrical measurements. B.W. and E.W. carried out the AFM and KPFM measurements. Y.S. and X.W. performed the Raman spectra measurements. All authors commented on the manuscript.

Funding: This work was financially supported by National Natural Science Foundation of China (11774191) and Fok Ying-Tong Education Foundation (161042).

Conflicts of Interest: The authors declare no conflict of interest.

References

1. Wang, Q.H.; Kalantar-Zadeh, K.; Kis, A.; Coleman, J.N.; Strano, M.S. Electronics and Optoelectronics of Two-Dimensional Transition Metal Dichalcogenides. *Nat. Nanotechnol.* **2012**, *7*, 699–712. [[CrossRef](#)] [[PubMed](#)]
2. Jariwala, D.; Sangwan, V.K.; Lauhon, L.J.; Marks, T.J.; Hersam, M.C. Emerging Device Applications for Semiconducting Two-Dimensional Transition Metal Dichalcogenides. *ACS Nano* **2014**, *8*, 1102–1120. [[CrossRef](#)] [[PubMed](#)]
3. Jariwala, D.; Marks, T.J.; Hersam, M.C. Mixed-dimensional Van der Waals Heterostructures. *Nat. Mater.* **2017**, *16*, 170–181. [[CrossRef](#)] [[PubMed](#)]
4. Nourbakhsh, A.; Zubair, A.; Dresselhaus, M.S.; Palacios, T. Transport Properties of a MoS₂/WSe₂ Heterojunction Transistor and Its Potential for Application. *Nano Lett.* **2016**, *16*, 1359–1366. [[CrossRef](#)] [[PubMed](#)]
5. Ceballos, F.; Bellus, M.Z.; Chiu, H.Y.; Zhao, H. Ultrafast Charge Separation and Indirect Exciton Formation in a MoS₂-MoSe₂ van der Waals Heterostructure. *ACS Nano* **2014**, *8*, 12717–12724. [[CrossRef](#)] [[PubMed](#)]
6. Chen, H.L.; Wen, X.W.; Zhang, J.; Wu, T.M.; Gong, Y.J.; Zhang, X.; Yuan, J.T.; Yi, C.Y.; Lou, J.; Ajayan, P.M.; et al. Ultrafast Formation of Interlayer Hot Excitons in Atomically Thin MoS₂/WS₂ Heterostructures. *Nat. Commun.* **2016**, *7*, 12512. [[CrossRef](#)] [[PubMed](#)]
7. Tran, K.; Moody, G.; Wu, F.C.; Lu, X.B.; Choi, J.; Kim, K.; Rai, A.; Sanchez, D.A.; Quan, J.M.; Singh, A.; et al. Evidence for Moire Excitons in van der Waals Heterostructures. *Nature* **2019**, *567*, 71–75. [[CrossRef](#)] [[PubMed](#)]
8. Chen, S.W.; Han, Z.; Elahi, M.M.; Habib, K.M.M.; Wang, L.; Wen, B.; Gao, Y.D.; Taniguchi, T.; Watanabe, K.; Hone, J.; et al. Electron Optics with p-n Junctions in Ballistic Graphene. *Science* **2016**, *353*, 1522–1525. [[CrossRef](#)]
9. Britnell, L.; Ribeiro, R.M.; Eckmann, A.; Jalil, R.; Belle, B.D.; Mishchenko, A.; Kim, Y.J.; Gorbachev, R.V.; Georgiou, T.; Morozov, S.V.; et al. Strong Light-Matter Interactions in Heterostructures of Atomically Thin Films. *Science* **2013**, *340*, 1311–1314. [[CrossRef](#)]
10. Wang, F.; Wang, Z.X.; Xu, K.; Wang, F.M.; Wang, Q.S.; Huang, Y.; Yin, L.; He, J. Tunable GaTe-MoS₂ van der Waals p-n Junctions with Novel Optoelectronic Performance. *Nano Lett.* **2015**, *15*, 7558–7566. [[CrossRef](#)]
11. Lee, C.H.; Lee, G.H.; van der Zande, A.M.; Chen, W.C.; Li, Y.L.; Han, M.Y.; Cui, X.; Arefe, G.; Nuckolls, C.; Heinz, T.F.; et al. Atomically Thin p-n Junctions with van der Waals Heterointerfaces. *Nat. Nanotechnol.* **2014**, *9*, 676–681. [[CrossRef](#)] [[PubMed](#)]
12. Furchi, M.M.; Pospischil, A.; Libisch, F.; Burgdorfer, J.; Mueller, T. Photovoltaic Effect in an Electrically Tunable van der Waals Heterojunction. *Nano Lett.* **2014**, *14*, 4785–4791. [[CrossRef](#)] [[PubMed](#)]
13. Wang, B.; Yang, S.X.; Wang, C.; Wu, M.H.; Huang, L.; Liu, Q.; Jiang, C.B. Enhanced Current Rectification and Self-Powered Photoresponse in Multilayer p-MoTe₂/n-MoS₂ van der Waals Heterojunctions. *Nanoscale* **2017**, *9*, 10733–10740. [[CrossRef](#)] [[PubMed](#)]
14. Chen, Y.; Wang, X.D.; Wu, G.J.; Wang, Z.; Fang, H.H.; Lin, T.; Sun, S.; Shen, H.; Hu, W.D.; Wang, J.L.; et al. High-Performance Photovoltaic Detector Based on MoTe₂/MoS₂ Van der Waals Heterostructure. *Small* **2018**, *14*, 1703293. [[CrossRef](#)] [[PubMed](#)]
15. Pezeshki, A.; Hossein, S.; Shokouh, H.; Nazari, T.; Oh, K.; Im, S. Electric and Photovoltaic Behavior of a Few-Layer α -MoTe₂/MoS₂ Dichalcogenide Heterojunction. *Adv. Mater.* **2016**, *28*, 3216–3222. [[CrossRef](#)] [[PubMed](#)]
16. Choi, K.; Lee, Y.T.; Min, S.W.; Lee, H.S.; Nam, T.; Kim, H.; Im, S. Direct Imprinting of MoS₂ Flakes on a Patterned Gate for Nanosheet Transistors. *J. Mater. Chem. C* **2013**, *1*, 7803–7807. [[CrossRef](#)]

17. Nam, D.; Lee, J.U.; Cheong, H. Excitation Energy Dependent Raman Spectrum of MoSe₂. *Sci. Rep.* **2015**, *5*, 17113. [[CrossRef](#)] [[PubMed](#)]
18. Lezama, I.G.; Arora, A.; Ubaldini, A.; Barreateau, C.; Giannini, E.; Potemski, M.; Morpurgo, A.F. Indirect-to-Direct Band Gap Crossover in Few-Layer MoTe₂. *Nano Lett.* **2015**, *15*, 2336–2342. [[CrossRef](#)]
19. Kang, J.; Tongay, S.; Zhou, J.; Li, J.B.; Wu, J.Q. Band Offsets and Heterostructures of Two-Dimensional Semiconductors. *Appl. Phys. Lett.* **2013**, *102*, 012111. [[CrossRef](#)]
20. Tongay, S.; Zhou, J.; Ataca, C.; Lo, K.; Matthews, T.S.; Li, J.B.; Grossman, J.C.; Wu, J.Q. Thermally Driven Crossover from Indirect toward Direct Bandgap in 2D Semiconductors: MoSe₂ versus MoS₂. *Nano Lett.* **2012**, *12*, 5576–5580. [[CrossRef](#)]
21. Ruppert, C.; Aslan, O.B.; Heinz, T.F. Optical Properties and Band Gap of Single- and Few-Layer MoTe₂ Crystals. *Nano Lett.* **2014**, *14*, 6231–6236. [[CrossRef](#)] [[PubMed](#)]
22. Li, Y.T.; Wang, Y.; Huang, L.; Wang, X.T.; Li, X.Y.; Deng, H.X.; Wei, Z.M.; Li, J.B. Anti-Ambipolar Field-Effect Transistors Based On Few-Layer 2D Transition Metal Dichalcogenides. *ACS Appl. Mater. Inter.* **2016**, *8*, 15574–15581. [[CrossRef](#)] [[PubMed](#)]
23. Wang, F.; Yin, L.; Wang, Z.X.; Xu, K.; Wang, F.M.; Shifa, T.A.; Huang, Y.; Jiang, C.; He, J. Configuration-Dependent Electrically Tunable Van der Waals Heterostructures Based on MoTe₂/MoS₂. *Adv. Funct. Mater.* **2016**, *26*, 5499–5506. [[CrossRef](#)]
24. Liu, Y.; Weiss, N.O.; Duan, X.D.; Cheng, H.C.; Huang, Y.; Duan, X.F. Van der Waals Heterostructures and Devices. *Nat. Rev. Mater.* **2016**, *1*, 16042. [[CrossRef](#)]
25. Shockley, W. The Theory of P-N Junctions in Semiconductors and P-N Junction Transistors. *Bell Syst. Tech. J.* **1949**, *28*, 435–489. [[CrossRef](#)]
26. Hao, J.H.; Gao, J.; Wang, Z.; Yu, D.P. Interface Structure and Phase of Epitaxial SrTiO₃ (110) Thin Films Grown Directly on Silicon. *Appl. Phys. Lett.* **2005**, *87*, 131908. [[CrossRef](#)]
27. Yang, Z.B.; Huang, W.; Hao, J.H. Determination of Band Alignment of Pulsed-Laser-Deposited Perovskite Titanate/III-V Semiconductor Heterostructure using X-ray and Ultraviolet Photoelectron Spectroscopy. *Appl. Phys. Lett.* **2013**, *103*, 031919. [[CrossRef](#)]
28. Schein, F.L.; von Wenckstern, H.; Grundmann, M. Transparent p-CuI/n-ZnO Heterojunction Diodes. *Appl. Phys. Lett.* **2013**, *102*, 092109. [[CrossRef](#)]
29. Zeng, L.H.; Wang, M.Z.; Hu, H.; Nie, B.; Yu, Y.Q.; Wu, C.Y.; Wang, L.; Hu, J.G.; Xie, C.; Liang, F.X.; et al. Monolayer Graphene/Germanium Schottky Junction as High-Performance Self-Driven Infrared Light Photodetector. *ACS Appl. Mater. Inter.* **2013**, *5*, 9362–9366. [[CrossRef](#)]
30. Wu, D.; Jiang, Y.; Zhang, Y.G.; Li, J.W.; Yu, Y.Q.; Zhang, Y.P.; Zhu, Z.F.; Wang, L.; Wu, C.Y.; Luo, L.B.; et al. Device Structure-Dependent Field-Effect and Photoresponse Performances of p-type ZnTe:Sb Nanoribbons. *J. Mater. Chem.* **2012**, *22*, 6206–6212. [[CrossRef](#)]
31. Kung, S.C.; van der Veer, W.E.; Yang, F.; Donavan, K.C.; Penner, R.M. 20 μs Photocurrent Response from Lithographically Patterned Nanocrystalline Cadmium Selenide Nanowires. *Nano Lett.* **2010**, *10*, 1481–1485. [[CrossRef](#)] [[PubMed](#)]
32. Choi, W.; Cho, M.Y.; Konar, A.; Lee, J.H.; Cha, G.B.; Hong, S.C.; Kim, S.; Kim, J.; Jena, D.; Joo, J.; et al. High-Detectivity Multilayer MoS₂ Phototransistors with Spectral Response from Ultraviolet to Infrared. *Adv. Mater.* **2012**, *24*, 5832–5836. [[CrossRef](#)] [[PubMed](#)]
33. Xu, H.; Wu, J.X.; Feng, Q.L.; Mao, N.N.; Wang, C.M.; Zhang, J. High Responsivity and Gate Tunable Graphene-MoS₂ Hybrid Phototransistor. *Small* **2014**, *10*, 2300–2306. [[CrossRef](#)] [[PubMed](#)]
34. Ahn, J.; Jeon, P.J.; Raza, S.R.A.; Pezeshki, A.; Min, S.W.; Hwang, D.K.; Im, S. Transition Metal Dichalcogenide Heterojunction PN Diode toward Ultimate Photovoltaic Benefits. *2D Mater.* **2016**, *3*, 045011. [[CrossRef](#)]
35. Wang, P.; Liu, S.S.; Luo, W.J.; Fang, H.H.; Gong, F.; Guo, N.; Chen, Z.G.; Zou, J.; Huang, Y.; Zhou, X.H.; et al. Arrayed Van Der Waals Broadband Detectors for Dual-Band Detection. *Adv. Mater.* **2017**, *29*, 1604439. [[CrossRef](#)] [[PubMed](#)]

36. Lu, M.Y.; Chang, Y.T.; Chen, H.J. Efficient Self-Driven Photodetectors Featuring a Mixed-Dimensional van der Waals Heterojunction Formed from a CdS Nanowire and a MoTe₂ Flake. *Small* **2018**, *14*, 1802302. [[CrossRef](#)] [[PubMed](#)]
37. Pospischil, A.; Furchi, M.M.; Mueller, T. Solar-energy Conversion and Light Emission in an Atomic Monolayer p-n Diode. *Nat. Nanotechnol.* **2014**, *9*, 257–261. [[CrossRef](#)] [[PubMed](#)]



© 2019 by the authors. Licensee MDPI, Basel, Switzerland. This article is an open access article distributed under the terms and conditions of the Creative Commons Attribution (CC BY) license (<http://creativecommons.org/licenses/by/4.0/>).